

# Adaptive Slater Koster Parameters: Crossing Oxidation States with Density Functional Tight Binding

Yihua Song,<sup>1</sup> Artem Samtsevych,<sup>1</sup> Anton Beiersdorfer,<sup>1</sup> Tobias  
Melson,<sup>2</sup> Christoph Scheurer,<sup>1</sup> Karsten Reuter,<sup>1</sup> and Chiara Panosetti<sup>1,\*</sup>

<sup>1</sup>*Fritz Haber Institute of the Max Planck Society, Faradayweg 4-6, 14195 Berlin, Germany*

<sup>2</sup>*Max Planck Computing and Data Facility, Gießenbachstraße 2, 85748 Garching b. München, Germany*

(Dated: May 20, 2026)

We propose to adapt the confined pseudo-atomic orbitals underpinning the precalculated Slater-Koster (SK) interaction tables in Density Functional Tight Binding (DFTB) to local atomic environments. We demonstrate significant improvement in electronic structure and energetics in the application to a partially oxidized Ni surface and Li insertion into graphite, where we assign optimal SK parameters to metal atoms in different oxidation states. Further analysis reveals the smoothness of the SK integrals across the varying oxidation states. Exploiting this, we introduce a site-resolved machine-learning scheme for fully adaptive DFTB. Using atomic descriptors and simple regression architectures already established in the context of machine-learning interatomic potentials, our scheme achieves 95% band-structure accuracy across all Ni–O binary compositions in the Materials Project.

As a stationary point approximation to density-functional theory (DFT), Density Functional Tight Binding (DFTB) [1] builds on ideas originating from the work of Slater and Koster [2] and the Foulkes-Haydock interpretation of tight binding [3], developed by Seifert, Porezag and Elstner [1, 4, 5] into the simple total energy formula:

$$E_{\text{tot}} = E_{\text{el}} + E_{\text{rep}} \quad . \quad (1)$$

Here,  $E_{\text{el}}$  is a parameterized electronic energy and the so-called repulsive energy  $E_{\text{rep}}$  represents a correction including the short-range nuclear repulsion as well as all the contributions not captured by the approximated electronic energy. In successively more sophisticated formulations,  $E_{\text{el}}$  takes the form of increasing orders of expansion around a reference non-interacting density. In the zeroth-order DFTB0 (often also called DFTB1) [4, 5],  $E_{\text{el}}$  is the so-called band-structure energy  $E_{\text{BS}}$ , where the non-self-consistent interaction is pre-calculated in a two-center approximation by solving a set of generalized eigenvalue equations using a minimal atomic-centered valence basis set under a parametric confinement, and tabulated in so called Slater-Koster (SK) integrals. This allows to access the electronic structure without painfully solving expensive self-consistent field equations at runtime. In the second- and third-order formulations (DFTB2/3 [1, 6]),  $E_{\text{BS}}$  is augmented with a charge-dependent Coulomb term  $E_{\text{coul}}$ . These formulations, also referred to as self-consistent-charge DFTB (SCC-DFTB), are nowadays the most widely used, with freely available simulation packages such as `df-tb+` [7]. More details are discussed in the End-Matter. With decades of development, DFTB has emerged as a leading semi-empirical method in large-scale theoretical research as it offers an excellent compromise between cost-effectiveness and accessible electronic structure accuracy [8, 9], enabling modelling of systems with thousands of atoms while preserving the description of essential quantum interactions, such as electron correlations and charge fluctuations [1]. Consequently, DFTB has demonstrated effectivity and versatility in applications ranging from molecular to materials simulations.

However, despite higher-order expansions, intrinsic limitations persist due to approximations and parameterization challenges [7]. For instance, previous studies highlighted the inadequacy of a single repulsive fit in both organic [10] and solid state [11] systems. While extended tuning [12, 13] and machine learning (ML) or many-body approaches [11, 14–16] provide partial solutions, repulsive fitting only corrects the total energy and forces, not the electronic structure. The minimal basis set and parametric nature of the precalculated interaction tables struggle in complex local environments [17], especially in systems with rich redox chemistry and massive charge transfer, like nickel oxides in various coordination types [18]. Analogously to the repulsion, a single, per-element fit of the electronic interaction—neglecting local environment subtleties—limits DFTB’s applicability to complex materials, especially those requiring accurate description of atomic charges and electronic features near the Fermi level. Recent efforts have begun to address this limitation through ML. Differentiable programming frameworks have enabled the optimization of DFTB electronic parameters, including environment-dependent compression radii, with demonstrated success for molecular systems and periodic solids with point defects [19–21]. Direct learning of tight-binding Hamiltonians [22, 23] and many-body corrections [24] have also been explored. However, these approaches have so far been applied to chemically homogeneous systems where the environmental variation is predominantly geometric rather than chemical in nature. Building on this progress, we here target systems where chemical heterogeneity—specifically, coexisting oxidation states of the same species—renders a single electronic parameterization fundamentally inadequate.

In this Letter, we show that in such systems, optimal confinement parameters respond systematically, decomposably and interpretably to both spatial and chemical factors, establishing the physical foundation for a site-resolved adaptive DFTB scheme. Starting with a simple rationalization in terms of discrete atomic types and using a mindfully chosen prototype system, we clearly demonstrate the significant improve-

ment in the electronic structure near the Fermi level. Scanning tunneling microscopy (STM) simulations of a stepped, partially oxidized Ni surface and exemplary reaction paths for lithium insertion into graphite demonstrate the broad applicability of the scheme. Crucially, the observed smoothness of SK parameters across chemical environments not only ensures physical interpretability but allows us to finally introduce a general ML scheme for continuous adaptation beyond the discrete picture, offering a data-efficient route to DFT-level accuracy in large-scale atomistic simulations.

To understand why the DFTB parameters intrinsically need local environment adaptation, we shall first briefly discuss some elements of DFTB parameterization. The two interaction terms in eq. (1) are routinely parameterized separately. The repulsion is parameterized by minimizing the deviation in force residues between DFT and repulsion-less DFTB. For long considered challenging, repulsive fitting is now largely facilitated by ML [14–16]. Hence, we turn our attention to the electronic parameterization, which is often oversimplified. The generalized Kohn-Sham equation [25] in a tight-binding ansatz can be written as follows:

$$\sum_{\nu}^M c_{\nu i} (H_{\mu\nu} - \varepsilon_i S_{\mu\nu}) = 0, \quad \forall \mu, i; \quad (2)$$

$$H_{\mu\nu} = \langle \varphi_{\mu} | \hat{H}_0 | \varphi_{\nu} \rangle + \frac{1}{2} S_{\mu\nu} \sum_{\xi}^N (\gamma_{\alpha\xi} + \gamma_{\beta\xi}) \Delta q_{\xi} \quad (3)$$

$$= H_{\mu\nu}^0 + H_{\mu\nu}^1, S_{\mu\nu} = \langle \varphi_{\mu} | \varphi_{\nu} \rangle, \quad \forall \mu \in \alpha, \nu \in \beta$$

where the two-center Hamiltonian  $H_{\mu\nu}$  and overlap matrix elements  $S_{\mu\nu}$  are pre-calculated following the Slater-Koster method [2] and stored in integral tables. The matrix elements are calculated using a parameterized basis, with  $\mu$  and  $\nu$  representing non-orthogonal pseudo-atomic orbitals at atoms  $\alpha$  and  $\beta$ . These are obtained from DFT calculations of spherical symmetric spin-unpolarized neutral atoms by solving:

$$\left( -\frac{1}{2} \nabla^2 + V_{\text{KS}}^{\text{eff}} [n_{\text{atomic}}] + V_{\text{conf}} \right) \varphi_{\nu} = \varepsilon \varphi_{\nu}, \quad (4)$$

where  $V_{\text{conf}}$  is a confinement potential applied to mimic the compression of wave functions upon bonding. This confinement (along with, optionally, an additional confinement for the atomic densities  $n_{\text{atomic}}$ ) is tuned until selected electronic properties are reproduced, usually band structures of simple solids. In standard parameterization approaches, for a given set of atomic species, the confinement potential is optimized once (single-fit) to yield, at best, a compromise across the target chemical compositions. However, one could argue that the confinement potential acts as a static correction to the effective potential  $V_{\text{KS}}^{\text{eff}}$  in eq. (4), to closely mimic the localization behavior of atomic orbitals in the realistic environment. Accordingly, we propose that each  $\varphi_{\nu}$  should be associated with a uniquely parameterized confinement potential that encodes tight-binding perturbations from the surrounding environment into the localized basis. In eq. (3),  $H_{\mu\nu}$  is expanded into a non-interacting  $H_{\mu\nu}^0$  contribution (core of the DFTB0 method) and

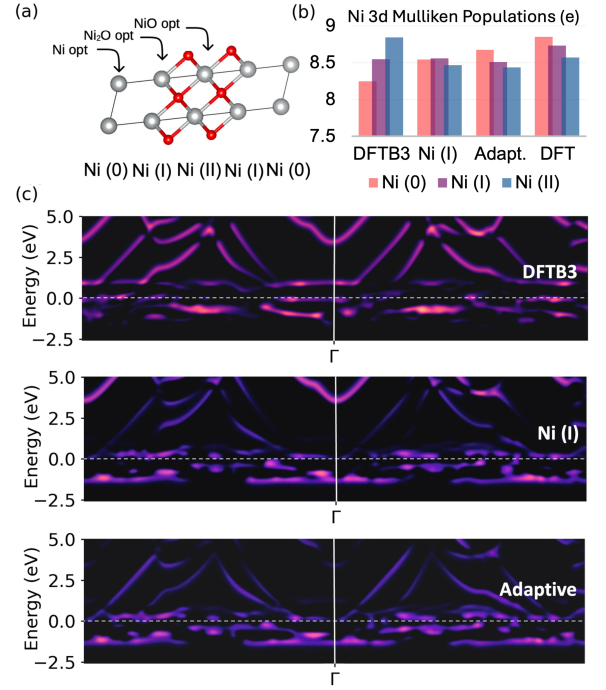


FIG. 1. (a) Structure of the conceptual Ni<sub>4</sub>O<sub>2</sub> system containing all three Ni oxidation states. (b) Mulliken population analysis for Ni 3d in this system, as well as (c) Gaussian difference maps. Compared in (b) and (c) are calculations done with published DFTB3 parameters [18], with optimal Ni(I) parameters applied globally to all Ni atoms, and with the adaptive approach using optimized parameters for each Ni oxidation state. In the difference maps, less residual coloring represents improved agreement with the DFT reference band structure (see text). The explicit band structures are reported in the EndMatter.

a second-order correction  $H_{\mu\nu}^1$  (core of the DFTB2 method). The latter represents the Coulomb interaction  $E_{\text{coul}}$  [1], where the screening terms  $\gamma$  depend on Hubbard parameters  $U$ . In the third-order DFTB3 [6], the Hubbard parameters are allowed to vary to improve the description of  $\gamma$  for polarized and charged systems. As such, modifications to  $\gamma$  (either via DFTB3 or a hypothetical adaptive variation of  $U$ ) play the same role as the adaptation of SK integrals, as we propose. However, acting on the SK integrals presents multiple advantages. First, it improves the localization behavior of the zeroth-order Hamiltonian. Second, an improved zeroth-order (hence most dominant) interaction should be more accurate than applying a third-order correction. Third,  $V_{\text{conf}}$  is the only truly empirical element in  $E_{\text{el}}$ , while  $U$  values can be calculated from first principles and carry direct physical meaning. Thus, in our view, their fully adaptive variation beyond DFTB3 is less justified than adapting the confinements.

To practically illustrate the limitation of a single-fit confinement in systems with coexisting different local environments, we choose nickel oxides with general formula NiO<sub>x</sub> and investigate the variation of optimal parameters across oxidation states. Aside from the technological relevance of nickel oxide for catalysis, magnetism and polaron research [26–28],

this choice is motivated by the fact that the conservation of the bulk cell shape from Ni to NiO isolates the oxidation effect from geometric changes. Let us first focus on bulk Ni, NiO, and an intermediate Ni<sub>2</sub>O structure, modeled by removing one oxygen atom from the (2 × 1 × 1) supercell of NiO, as shown in Fig. S3. Nickel atoms in these structures have formal oxidation states Ni(0), Ni(I) and Ni(II), respectively. Specific parameterizations for each are obtained using our newly developed optimization code DSKO [29], with non-spin-polarized NiO<sub>x</sub> DFT-PBE [30] band structures as references (to ensure comparability with published parameters but without losing generality, cf. SM for details). Employed is the most used confinement potential, the power law model, defined as  $V_{\text{conf}}(r) = (\frac{r}{r_0})^k$ . Typically, the dominant parameter is the onset radius  $r_0$ , whereas  $k$  merely modulates the decay of the confined orbitals. As expected, the resulting optimal parameters are sensitive to local environments, with the dominant  $r_{0,\text{Ni}_{3d}}$  parameter increasing from 3.49 (Ni) to 3.87 (Ni<sub>2</sub>O) to 4.01 (NiO) Bohr.

It is then natural to hypothesize that, in principle, assigning optimal parameters to each atom in a complex system should yield a finer description of the electronic structure. To demonstrate the advantages of this concept in an intuitive discrete-type picture, we design a fictitious "all-types-in-one" Ni<sub>4</sub>O<sub>2</sub> system. This system is of formal Ni<sub>2</sub>O stoichiometry, obtained by removing two O atoms from a NiO (4 × 1 × 1) supercell. It simultaneously contains all three types of Ni atoms in one structure within Ni(0)-Ni(I)-O-Ni(II)-O-Ni(I) chains as shown in Fig. 1a. Next to the actual DFT reference, we compare to two conventional DFTB single-point calculations where all Ni atoms are assigned the same SK parameters, once published DFTB3 parameters [18, 31] and once our optimal DFTB2 parameters for the intermediate Ni(I) oxidation state of the formal system stoichiometry. In our adaptive approach, we instead use the respective optimal parameters for the Ni atoms in the different oxidation states. As shown in Fig. 1b, the latter approach yields indeed more accurate Mulliken charge populations. In fact, it is the only one that reproduces the relative ordering of the DFT reference charges for the three oxidation states. Also improved is the band structure, in particular around the Fermi level. Deferring a more detailed discussion to EndMatter, we demonstrate the latter improvement in Fig. 1 with Gaussian difference maps. In this scheme, we apply a Gaussian broadening to both the DFT reference and the DFTB band structure and then subtract both from each other. A perfect band reproduction would yield a fully black difference map, with residual discrepancies readily apparent as lighter colored regions. Clearly, the adaptive calculation using specifically assigned parameters reproduces the bands better than both the conventional DFTB3 with published parameters [18, 31] and the DFTB2 calculation globally using the Ni(I) parameters.

To demonstrate the impact of an adaptive DFTB approach in practical atomistic modelling applications, we present scanning tunneling microscopy (STM) simulations as prototypical use case drawing on a faithful description of the electronic

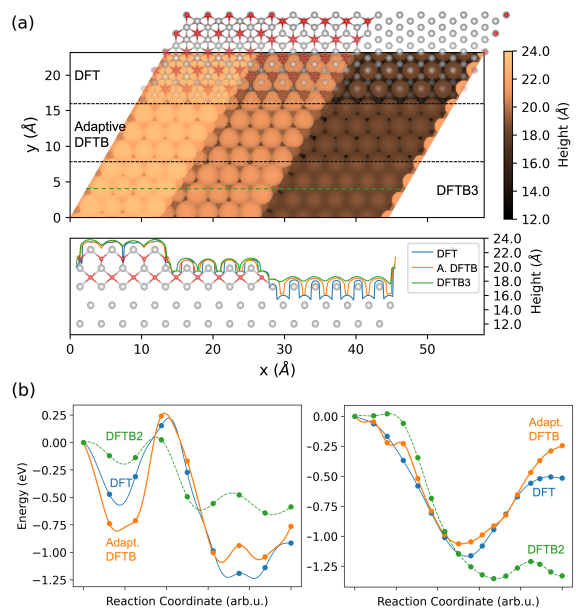


FIG. 2. Comparison of adaptive DFTB calculations against the DFT reference and conventional DFTB2/3 (see text) for two application cases. (a) Tersoff-Hamann type STM simulations of a Ni(111) surface, partially covered with one and two layers of NiO surface oxide (1 V bias, 0.55 pA, corresponding to an iso-density of  $4.69 \times 10^{-6} e/\text{\AA}^3$  [32]). With both panels sharing the same  $x$ -axis, the upper panel shows a top view of the simulated STM image at the different levels of theory. The bottom panel shows a side view of the surface structure, overlaid with an STM line scan along the green dashed lines in (a). (c) Minimum energy paths for Li insertion into graphite through the zigzag (left) and armchair (right) terminations.

density around the Fermi level, and reaction paths as prototypical use case requiring an accurate description of total energy and forces. The prior Tersoff-Hamann type simulations are performed for a Ni(111) surface partially covered with one and two layers of NiO surface oxide, in total producing a stepped surface as shown in Fig. 2a. Comparing against the DFT reference and DFTB3 with global parameters, we note that in the prior application DFTB inherently produces slightly more diffuse charge densities than DFT. However, the orbital compression effects induced by different degrees of oxidation at each step are effectively only captured by the adaptive approach, thus excelling in the description of localized electronic features. As reaction pathways we focus on lithium insertion into graphite, where the penetrating Li atom evolves into progressively higher oxidation states. Specifically, we start from relaxed geometries and energetics along the minimum energy path obtained with nudged elastic band [33] calculations performed with published DFTB2 parameters [34, 35]. We then perform single-point calculations at DFT and adaptive DFTB level, where for the latter we approximately take as optimized SK parameters for interfacial Li the average of the optimized SK parameters for metallic and intercalated Li, cf. SM for details. Fig. 2b reveals also in this case a superior performance of the adaptive approach,

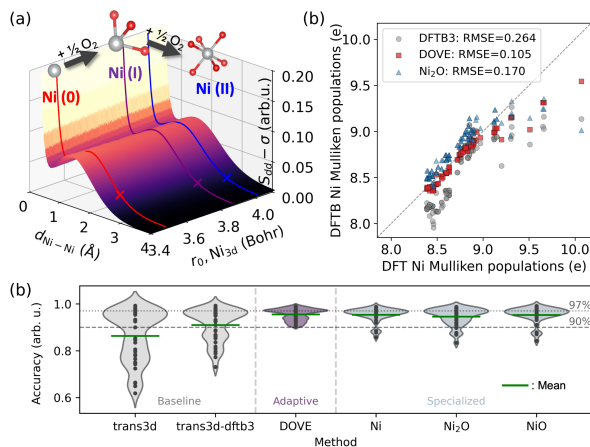


FIG. 3. (a) Plot of the exemplary  $S_{dd-\sigma}$  SK integral as a function of the interatomic distance  $d_{Ni-Ni}$  and the onset radius  $r_{0,Ni3d}$  of the confinement potential as obtained from the DSKO optimization for Ni<sub>2</sub>O. The variation with respect to  $r_{0,Ni3d}$  is smooth, save for the noise originating from the sampling of the other, non-dominant, parameters. Optimal  $r_{0,Ni3d}$  are highlighted for pure Ni (red line), Ni<sub>2</sub>O (purple line) and NiO (blue line), and the crosses mark the specific SK parameter values taken at the  $d_{Ni-Ni}$  corresponding to the respective relaxed unit-cell geometry. (b) Ni (valence) Mulliken population correlation between DFT (LOBSTER [36]) and DFTB across the same test set in (c). (c) DFTB band structure accuracy (see End-Matter) for 37 Ni-O binary structures from the Materials Project.

with conventional DFTB in fact grossly misrepresenting the insertion barrier.

While encouraging, this proof of concept is vain in practice. If one were to obtain parameters for any possible atomic type in a complex simulation from numerical optimization, the resulting parameterization effort would render the adaptive approach impractical for realistic applications. Fortunately, the progressive increase of the dominant  $r_{0,Ni3d}$  onset radius hints at the fact that, while intuitive, the difference in parameter optimality can be rigorously rationalized within DFTB theory and subsequently generalized. A larger  $r_0$  implies a weaker  $V_{conf}$  correction to the atomic effective potential in eq. (4). This corresponds to a more diffuse orbital, whose energetic behavior is closer to a free atom Hamiltonian, and *vice versa*. Here, the increasing  $r_{0,Ni3d}$  suggests a more diffuse orbital in higher oxidation states, while the oxidation process, intuitively, should introduce orbital compression [17]. This apparent contradiction is discussed in detail in the EndMatter (Appendix D), with a systematic investigation revealing an interpretable correlation between chemical (oxidation state) and spatial (cell volume) factors. Notably, the confinement onset radius in the NiO<sub>x</sub> decomposes approximately as  $r_0 \approx \alpha l + \beta$ , with  $\alpha$  capturing the spatial (lattice) dependence and  $\beta$  encoding the chemical (oxidation) shift. Crucially, this systematic and decomposable response of optimal DFTB parameters to physical variables establishes a well-defined mapping from local chemical environments to numerical SK parameters, and potentially to broader physical properties, provided that such a relationship is smooth. We thus proceed to investigate the

evolution of SK integrals, the electronic coupling quantities embedded in the equations governing DFTB. Fig. 3 summarizes this evolution exemplarily for the  $S_{dd-\sigma}$  SK overlap integral, which determines the Ni-Ni  $3d-3d$   $\sigma$  bonding interaction and is one of the quantities entering both terms of the sum in eq. (2) and the interacting SCC term in eq. (3). With analog findings for other SK parameters, the evolution is indeed smooth. This regularity motivates a simple but consequential approach for a fully adaptive DFTB scheme beyond discrete types by physically-informed ML. If the environment-to-parameter mapping is indeed well-behaved, then even a minimal regression model should be capable of predicting SK parameters for unseen configurations without material-specific re-optimization. We refer to this site-resolved prediction scheme as DOVE (DFTB Orbitals in Variable Environment).

The critical point is not the sophistication of the regression, which is deliberately kept simple, but that the physical regularity established above suffices to support predictive parameterization across distinct stoichiometries and structures within the configurational space with only a handful of reference data. Additionally, the smoothness of the SK integrals across confinements ensures well-conditioned overlap matrices in the mixed basis. We train a Gaussian process regression model with a modified [37, 38] atom-centered SOAP descriptor [39], to predict one-center confinement parameters on a compact set of 61 structures containing no more than 4 atoms each, selected from a dataset generated using modular evolutionary structure search [40] to maximally capture the diversity of spatial and chemical environments in Ni-O binary bulk systems (cf. SM). We then benchmark the band-structure agreement across all Ni-O binary compounds with varying oxidation states from bulk Ni to Ni (VI) in the Materials Project [41], none of which are included in the training set, comparing all methods discussed in this work using an accuracy score based on the Gaussian difference, as defined in the EndMatter. Fig. 3b confirms that the improved band-structure accuracy translates into more faithful Ni Mulliken charge populations, with DOVE consistently closest to the DFT reference across the full range of oxidation states (cf. SM). As shown in Fig. 3c, our optimized single-type parameters already yield overall accuracy above 80%, but DOVE reaches 95% average accuracy with a median near 97%, outperforming both the published parameters and our own single-type parameterizations. Further validation on held-out structures from the evolutionary dataset confirms the robustness of the approach (cf. SM). While atomic descriptors (e.g. SOAP [39], ACE [42]) can be employed to learn the confinements, the framework is immediately extensible to two-center descriptors (e.g. Allegro [43]) to directly learn the variation of SK integrals, thus skipping the on-the-fly reparameterization step, which albeit accelerated (cf. SM), adds some computational overhead. Of note, one may cluster local environments at any degree of granularity (from discrete to fully continuous) using fuzzy classifiers such as DECAF [38]. Indeed, the latter readily identifies the Ni oxidation states discussed in the above con-

ceptual Ni<sub>4</sub>O<sub>2</sub> system, as well as in the stepped Ni surface, as discrete, distinct environments (cf. SM).

In conclusion, we developed an adaptive DFTB approach that roots in the interpretation of the DFTB pseudo-atomic orbitals as static approximations of Kohn-Sham eigenstates. The latter suggests to locally tailor the employed confinement potentials to describe the varying orbital diffuseness in systems containing the same species in different chemical environments. In this work, we first provided a discrete proof-of-principle demonstration of this concept by assigning specifically optimized Slater-Koster parameters to atoms in different oxidation states. Although the presented applications are based on semi-local DFT references (for direct comparison with published parameters [31, 35]), the concept is independent of the choice of reference, thus our conclusions are not expected to change when fitting DFTB to higher-level functionals [44]. While recent ML approaches to semiempirical electronic structure have focused on improving parameterization accuracy within chemically homogeneous settings, the present work establishes the physical foundation of why parameters can—and must—vary across chemical environments. Once this regularity is established, even a minimal regression suffices, shifting the challenge from architectural complexity to physical understanding. The demonstrated smoothness of Slater-Koster parameters across oxidation environments paves the way to finer granularity, ultimately exploiting local atomic environment representations to predict SK parameters that continuously vary across compositions without sacrificing computational efficiency. We validate this route by showing that a machine-learned site-resolved parameterization trained on a small dataset reproduces DFT-level band structures accurately and transfers reliably across oxidation environments. Our results thus establish an adaptive, physically grounded, ML-driven DFTB framework capable of reliable and realistic electronic structure simulations.

We gratefully acknowledge funding through grants no. 03HY130H (AEM-Direkt), no. 03EW0015B (CatLab) and no. 03SF0785C (MacGyver) of the German Federal Ministry of Education and Research (BMBF) and the computational and data resources provided by the Max Planck Computing and Data Facility (MPCDF). We gratefully acknowledge valuable discussions with Dr. King Chun Lai, Dr. Andrew Wong, and Dr. Aditya Kumar.

The authors declare no competing interests.

*Data availability*—All the input files, scripts and relevant output files are available as a repository at [45].

---

\* panosetti@fhi.mpg.de

- [1] M. Elstner, D. Porezag, G. Jungnickel, J. Elsner, M. Haugk, T. Frauenheim, S. Suhai, and G. Seifert, *Phys. Rev. B* **58**, 7260 (1998).
- [2] J. C. Slater and G. F. Koster, *Phys. Rev.* **94**, 1498 (1954).
- [3] W. M. C. Foulkes and R. Haydock, *Phys. Rev. B* **39**, 12520 (1989).
- [4] G. Seifert, D. Porezag, and T. Frauenheim, *Int. J. Quantum Chem.* **58**, 185 (1996).
- [5] D. Porezag, T. Frauenheim, T. Köhler, G. Seifert, and R. Kaschner, *Phys. Rev. B* **51**, 12947 (1995).
- [6] M. Gaus, Q. Cui, and M. Elstner, *J. Chem. Theory Comput.* **7**, 931 (2011).
- [7] B. Hourahine, B. Aradi, V. Blum, F. Bonafé, A. Buccheri, C. Camacho, C. Cevallos, M. Y. Deshayé, T. Dumitric, A. Dominguez, S. Ehlert, M. Elstner, T. V. D. Heide, J. Hermann, S. Irle, J. J. Kranz, C. Köhler, T. Kowalczyk, T. Kubař, I. S. Lee, V. Lutsker, R. J. Maurer, S. K. Min, I. Mitchell, C. Negre, T. A. Niehaus, A. M. Niklasson, A. J. Page, A. Pecchia, G. Penazzi, M. P. Persson, J. Řezáč, C. G. Sánchez, M. Sternberg, M. Stöhr, F. Stuckenberg, A. Tkatchenko, V. W. Yu, and T. Frauenheim, *J. Chem. Phys.* **152**, 10.1063/1.5143190 (2020).
- [8] P. O. Dral, X. Wu, and W. Thiel, *J. Chem. Theory Comput.* **15**, 1743 (2019).
- [9] P. O. Dral, B. Hourahine, and S. Grimme, *J. Chem. Phys.* **160** (2024).
- [10] M. Gaus, A. Goetz, and M. Elstner, *J. Chem. Theory Comput.* **9**, 338 (2013).
- [11] A. K. Ammothum Kandy, E. Wadbro, B. Aradi, P. Broqvist, and J. Kullgren, *Journal of Chemical Theory and Computation* **17**, 1771–1781 (2021).
- [12] M. Hellström, K. Jorner, M. Bryngelsson, S. E. Huber, J. Kullgren, T. Frauenheim, and P. Broqvist, *J. Phys. Chem. C* **117**, 17004 (2013).
- [13] A. Fihey, C. Hettich, J. Touzeau, F. Maurel, A. Perrier, C. Köhler, B. Aradi, and T. Frauenheim, *J. Comput. Chem.* **36**, 2075 (2015).
- [14] C. Panosetti, A. Engelmann, L. Nemeč, K. Reuter, and J. T. Margraf, *J. Chem. Theory Comput.* **16**, 2181 (2020).
- [15] M. Stoöhr, L. Medrano Sandonas, and A. Tkatchenko, *J. Phys. Chem. Lett.* **11**, 6835 (2020).
- [16] N. Goldman, L. E. Fried, R. K. Lindsey, C. H. Pham, and R. Dettori, *J. Chem. Phys.* **158**, 144112 (2023).
- [17] C. Panosetti, Y. Lee, A. Samtsevych, and C. Scheurer, *J. Chem. Phys.* **158**, 224115 (2023).
- [18] M. Vujović, M. Huynh, S. Steiner, P. Garcia-Fernandez, M. Elstner, Q. Cui, and M. Gruden, *J. Comput. Chem.* **40**, 400 (2019).
- [19] G. Fan, A. McSloy, B. Aradi, C.-Y. Yam, and T. Frauenheim, *The Journal of Physical Chemistry Letters* **13**, 10132–10139 (2022).
- [20] A. McSloy, G. Fan, W. Sun, C. Hölzer, M. Friede, S. Ehlert, N.-E. Schütte, S. Grimme, T. Frauenheim, and B. Aradi, *The Journal of Chemical Physics* **158**, 10.1063/5.0132892 (2023).
- [21] W. Sun, G. Fan, T. van der Heide, A. McSloy, T. Frauenheim, and B. Aradi, *Journal of Chemical Theory and Computation* **19**, 3877–3888 (2023).
- [22] F. Hu, F. He, and D. J. Yaron, *Journal of Chemical Theory and Computation* **19**, 6185–6196 (2023).
- [23] Q. Gu, Z. Zhouyin, S. K. Pandey, P. Zhang, L. Zhang, and W. E. Nature Communications **15**, 10.1038/s41467-024-51006-4 (2024).
- [24] D. J. Burrill, C. Liu, M. G. Taylor, M. J. Cawkwell, D. Perez, E. R. Batista, N. Lubbers, and P. Yang, *Journal of Chemical Theory and Computation* **21**, 1089–1097 (2025).
- [25] W. Kohn and L. J. Sham, *Phys. Rev.* **140**, A1133 (1965).
- [26] A. Kubas, F. Hoffmann, A. Heck, H. Oberhofer, M. Elstner, and J. Blumberger, *J. Chem. Phys.* **140**, 104105 (2014).
- [27] M. Gaus, X. Lu, M. Elstner, and Q. Cui, *J. Chem. Theory Comput.* **10**, 1518 (2014).
- [28] M. Tadic, D. Nikolic, M. Panjan, and G. R. Blake, *J. Alloys Compd.* **647**, 1061 (2015).

- [29] A. Samtsevych, Y. Song, T. van der Heide, B. Aradi, B. Hourahine, R. Maurer, K. Reuter, C. Scheurer, and C. Panosetti, ChemRxiv 10.26434/chemrxiv-2025-4cmx9 (2025).
- [30] J. P. Perdew, K. Burke, and M. Ernzerhof, Phys. Rev. Lett. **77**, 3865 (1996).
- [31] G. Zheng, H. A. Witek, P. Bobadova-Parvanova, S. Irle, D. G. Musaev, R. Prabhakar, K. Morokuma, M. Lundberg, M. Elstner, C. Köhler, and T. Frauenheim, J. Chem. Theory Comput. **3**, 1349 (2007).
- [32] W. A. Hofer, A. S. Foster, and A. L. Shluger, Rev. Mod. Phys. **75**, 1287 (2003).
- [33] H. Jónsson, G. Mills, and K. W. Jacobsen, in *Classical and Quantum Dynamics in Condensed Phase Simulations* (World Scientific, 1998) p. 385–404.
- [34] C. Panosetti, S. B. Annies, C. Grosu, S. Seidlmayer, and C. Scheurer, J. Phys. Chem. A **125**, 691–699 (2021).
- [35] S. Annies, C. Panosetti, M. Voronenko, D. Mauth, C. Rahe, and C. Scheurer, Materials **14**, 6633 (2021).
- [36] R. Nelson, C. Ertural, J. George, V. L. Deringer, G. Hautier, and R. Dronskowski, Journal of Computational Chemistry **41**, 1931–1940 (2020).
- [37] A. P. Bartók, S. De, C. Poelking, N. Bernstein, J. R. Kermode, G. Csányi, and M. Ceriotti, Science Advances **3**, 10.1126/sciadv.1701816 (2017).
- [38] K. C. Lai, S. Matera, C. Scheurer, and K. Reuter, J. Chem. Phys. **159**, 024129 (2023).
- [39] A. P. Bartók, R. Kondor, and G. Csányi, Phys. Rev. B **87**, 184115 (2013).
- [40] J. M. Lombardi, F. Riccius, C. W. P. Pare, H. H. Heenen, K. Reuter, and C. Scheurer, ChemRxiv **2026** (2026), <https://chemrxiv.org/doi/pdf/10.26434/chemrxiv.15000180/v1>.
- [41] A. Jain, S. P. Ong, G. Hautier, W. Chen, W. D. Richards, S. Dacek, S. Cholia, D. Gunter, D. Skinner, G. Ceder, and K. a. Persson, APL Mater. **1**, 011002 (2013).
- [42] I. Batatia, S. Bätzner, D. P. Kovács, A. Musaelian, G. N. C. Simm, R. Drautz, C. Ortner, B. Kozinsky, and G. Csányi, Nat. Mach. Intell. **7**, 56 (2025).
- [43] A. Musaelian, S. Bätzner, A. Johansson, L. Sun, C. J. Owen, M. Kornbluth, and B. Kozinsky, Nat. Commun. **14**, 579 (2023).
- [44] T. van der Heide, B. Aradi, B. Hourahine, T. Frauenheim, and T. A. Niehaus, Phys. Rev. Mater. **7**, 063802 (2023).
- [45] Y. Song, Data Availability to Adaptive Slater Koster Parameters: Crossing Oxidation States with Density Functional Tight Binding (2026).
- [46] B. Hammer and J. Nørskov, in *Impact of Surface Science on Catalysis*, Advances in Catalysis, Vol. 45 (Academic Press, 2000) pp. 71–129.

## END MATTER

Appendix A: DFTB theory, total energy, and DFTB2 SCC. In Kohn-Sham density-functional theory [25], for a multi-electron system in a field of  $N$  nuclei at positions  $\vec{R}$ , the total energy can be written as a functional of the charge density  $n(\vec{r})$ . Within the tight binding ansatz [3], one can interpret the total energy as dependent on a small density fluctuation  $n(\vec{r}) = n_0(\vec{r}) + \delta n(\vec{r})$  around a reference density  $n_0(\vec{r})$  constructed by superposition of non-interacting atomic densities  $n_{\text{atomic}}$  (see 4). With a second order expansion of  $E_{\text{xc}}[n]$  at  $n_0$ ,

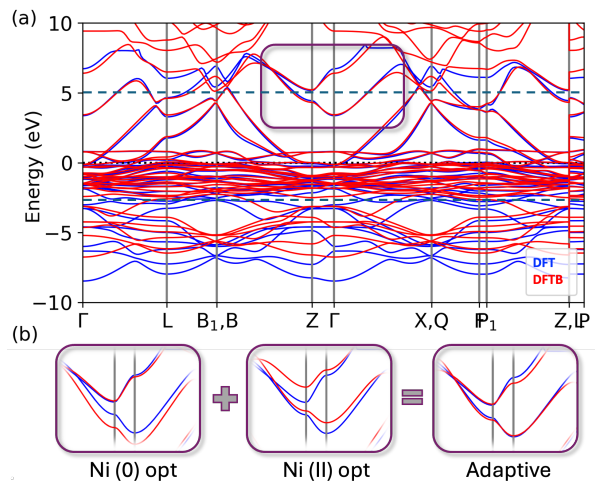


FIG. 4. (a)  $\text{Ni}_4\text{O}_2$  band structure comparison between DFT and DFTB with the adaptive approach. Green dashed lines indicate the energy range at which the band structure is truncated to construct the Gaussian difference maps. (b) Schematic representation of a simplified mechanism of improvement of the electronic properties in the adaptive approach. For the isolated band, the single-type confinement for Ni(I) and Ni(II) produces too large and too small dispersion, respectively, while the adaptive parameterization produces the correct dispersion.

a simple form for the total energy is obtained as:

$$\begin{aligned}
 E[n_0, \delta n] = & \sum_i^{\text{occ}} \langle \Psi_i | -\frac{1}{2} \nabla^2 + V_{KS} | \Psi_i \rangle \\
 & + \frac{1}{2} \int \int' \left[ \frac{n'_0 n_0}{|\vec{r} - \vec{r}'|} + \frac{\delta^2 E_{\text{XC}}}{\delta n \delta n'} \Big|_{n_0} \right] \delta n \delta n' \quad (\text{A.5}) \\
 & - \frac{1}{2} \int \int' \frac{n'_0 n_0}{|\vec{r} - \vec{r}'|} + E_{\text{XC}}[n_0] - \int V_{\text{XC}}[n_0] n_0 + E_{ii}
 \end{aligned}$$

where  $n$  is the electron density,  $V_H$  and  $V_{\text{xc}}$  are the Hartree and exchange-correlation potentials,  $E_{\text{xc}}[n]$  is the exchange-correlation functional, and  $E_{ii}$  accounts for the ion-ion repulsion interaction, with  $\int$  and  $\int'$  indicating  $\int d\vec{r}$  and  $\int d\vec{r}'$  respectively. The first summation term is normally referred to as the "band structure" energy  $E_{\text{BS}}$  and the second term as the Coulomb energy  $E_{\text{coul}}$ , and together they add up to the so-called electronic part of the interaction  $E_{\text{el}}$ . The remaining terms are lumped together into the so-called repulsive interaction  $E_{\text{rep}}$ . In the DFTB2 approach (cf. eq. (3)), the partial charges depend on the ground-state density, and the  $H_{\mu\nu}^1$  (hence the ground-state density) is expressed in terms of partial charges. This term is thus solved by self-consistently optimizing Mulliken partial charges [1].

Appendix B: A closer inspection of the band structure suggests a possible simplified mechanism by which the local parameterization improves the description of electronic properties. In Fig. 2 (c), the adaptive band prediction is compared with the band structures obtained from "single-type" parameters, which shows that the optimal Ni(0) and the optimal Ni(II) parameters produce slightly stretched and slightly com-

pressed bands respectively in the highlighted feature, while the adaptive parameterization produces the correct dispersion. Ni(0)-optimal parameters correspond to a globally less diffuse orbital, but yield a larger overlap at the relevant bond distance, while Ni(II)-optimal parameters correspond to a globally more diffuse orbital, but yield a smaller overlap at the relevant bond distance. As a result, consistently with "textbook" tight binding, a larger overlap corresponds to more dispersed bands, and *vice versa*.

Appendix C: The band structure of the  $\text{Ni}_4\text{O}_2$  trial system features multiple overlapping bands, making point-wise comparison between DFT and DFTB non-trivial. Conventional eigenvalue-based metrics such as the mean absolute error (MAE) can be misleading in such dense band manifolds, where topologically incorrect bands may coincidentally overlap in energy with reference states. We therefore introduce the Gaussian difference map — and derive from it a scalar *accuracy score* that captures band dispersion and local spectral features rather than individual eigenvalue coincidence, and is thus more sensitive to physically meaningful deviations near the Fermi level.

The Gaussian difference map is constructed as follows. The DFT reference and DFTB band structures are each truncated to a chosen energy window around the Fermi level ( $-2.5$  to  $+5.0$  eV for the  $\text{Ni}_4\text{O}_2$  analysis;  $-5$  to  $+5$  eV for the DOVE benchmark in Fig. 3. The wider window for the benchmark accommodates high-oxidation-state compounds whose principal near-Fermi features extend beyond  $-2.5$  eV; the accuracy ranking among methods is insensitive to this choice). Each band structure is then discretized on a uniform grid in  $(k, E)$  space, represented as a scalar intensity field, and broadened with a 2D Gaussian kernel  $\mathcal{G}_{\sigma_k, \sigma_E}$  with independent broadening widths  $\sigma_k$  and  $\sigma_E$  along the  $k$ -space and energy axes, respectively. Each grid point intensity is normalized by the maximum of the broadened intensity scale  $B_{\max}$ , rescaling all intensities to  $[0, 1]$ :

$$\tilde{B}_i = \frac{(\mathcal{G}_{\sigma_k, \sigma_E} * B)_i}{B_{\max}}. \quad (\text{A.6})$$

The point-wise absolute difference between the normalized DFT and DFTB spectra yields the Gaussian difference map. A perfect band reproduction produces a uniformly vanishing map; residual discrepancies appear as regions of finite intensity (cf. SM for technical details).

From the map we define the *accuracy score*

$$\mathcal{A} = 1 - \mathcal{E}, \quad \mathcal{E} = \frac{1}{N} \sum_{i=1}^N |\tilde{B}_i^{\text{DFTB}} - \tilde{B}_i^{\text{DFT}}|, \quad (\text{A.7})$$

where  $\mathcal{E}$  is the mean Gaussian error (MGE) averaged over all  $N$  grid points in the map. The score is bounded  $\mathcal{A} \in [0, 1]$ , with  $\mathcal{A} = 1$  corresponding to perfect reproduction. Results for the  $\text{Ni}_4\text{O}_2$  system are reported in Table I, alongside the conventional MAE for comparison. For completeness, a conventional MAE-based comparison across the Materials Project

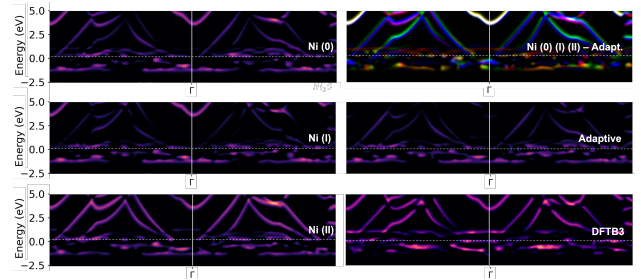


FIG. 5. Gaussian difference maps for  $\text{Ni}_4\text{O}_2$  calculated with different Ni DFTB parameters. The RGB figure represents the stacking of highlighted mismatch bands, which provides a joint picture of which features are most wrong and where. (R, G, B: single parameterization wrong in that spot, respectively as Ni 0, Ni (I) and Ni (II)).

benchmark is reported in the SM (Fig. S13), confirming that DOVE outperforms all other schemes also by this measure, albeit with less discriminating power between methods. Beyond the band-structure metric, Fig. 3c demonstrates that the accuracy score correlates with the fidelity of a ground-state electronic structure property: Ni Mulliken charges computed with DOVE agree more closely with the DFT reference (RMSE = 0.105 e) than those from any single-type scheme. This confirms that the Gaussian difference map captures physically meaningful improvements in the electronic structure, not merely a better visual fit.

	Ni (0)	Ni (I)	Ni (II)	DFTB3	Adaptive
MGE (%)	4.84	6.03	7.91	7.32	3.76
MAE (eV)	0.120	0.1495	0.162	0.134	0.0972

TABLE I. MGE and MAE for the  $\text{Ni}_4\text{O}_2$  band structures under different parametrization schemes.

More granular information is provided by RGB analysis as shown in Fig. 5. Here, Gaussian difference maps are constructed for each single type band structure with respect to the adaptive calculation and mapped onto red (Ni(0)), green (Ni(I)) and blue (Ni(II)) color channels. Areas where the single-type parameters struggle to describe the bands correctly are therefore highlighted in yellow, purple, cyan, or white, depending on which and how many single-type parameters deviate more from the adaptive approach for that particular feature. Notably, the white region indicates where the simple mechanism mentioned in Appendix B can be interpretably isolated.

Appendix D: To elucidate the relationship between the optimal DFTB parameters and the varying local environment, here specifically the oxidation state, we employ PDOS and  $d$ -band center analysis [46] to track the evolution of electronic properties (see SM for details). PDOS calculations in the  $\text{NiO}_x$  ( $x=0,0.5,1$ ) systems show a good fit with DFT calculations within our optimal parameters, as expected. The comparison of Ni- $3d$  PDOS in three  $\text{NiO}_x$  systems shows a more compressed  $d$  band in the oxidized NiO bulk, while part of

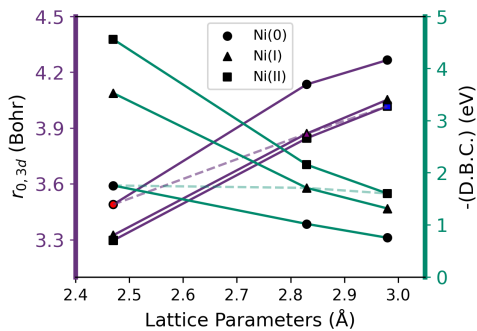


FIG. 6. DBC and optimal  $r_{0,Ni_{3d}}$  for nickel oxides systems in all three oxidation states and all three  $l_x$  lattice parameters. The three equilibrium systems are highlighted by color and connected with dashed lines.

the  $d$  electrons split into the inner shell due to the oxidation, which indicates a compression effect and charge transfer on the Ni  $d$  electrons from oxidation. However, the  $d$ -band center (DBC) analysis tells a different story.

The DBC of  $NiO_x$  bulk systems shows an increasing trend with the oxidation process, as shown in Fig. 6 (green dashed line), which implies a more populated  $d$  band with increasing oxidation state. This can also be interpreted as a state approaching more diffuse, interacting  $d$  orbitals—which is consistent with the pseudo-atomic basis within increasing  $r_{0,Ni_{3d}}$  parameters. We meet an apparent contradiction between orbital compression and diffuseness trends with oxidation.

The key lies in bulk cell expansion. Despite the simplicity of our prototype  $NiO_x$  systems, bulk volume—i.e., the equilibrium interaction distance—remains a crucial co-factor in

orbital interactions. The lattice parameter  $l$  increases with oxidation, from 2.47 Å (Ni) via 2.83 Å ( $Ni_2O$ ) to 2.97 Å ( $NiO$ ). Hence, we systematically investigate multiple trial systems within varying lattice parameters based on the original Ni(0), Ni(I) and Ni(II) motifs, and calculate their PDOS and DBC with DFT for uni-variate analysis. The green lines in Fig. 6 show that the DBC levels decrease with oxidation, which implies orbital compression, and increase with the enlarging cell, which indicates orbital diffuseness. The oxidation-induced charge transfer and the enlarged interaction distance counteract their respective compressive and diffusive "effects" on the DFTB pseudo-atomic orbital. This interplay may be envisioned as a pair of dancers maintaining a delicate equilibrium—pushing through oxidation-driven compression and pulling through increased cell strain—yielding a smoothly balanced evolution of electronic interaction (green dashed line). Inspired by the chemical trend observed in DBC analysis, we apply particle swarm optimization to parameterize those trial systems, probing the coupling of DFTB parameters with spatial and chemical environments. As Fig. 6 shows,  $r_{0,Ni_{3d}}$  (purple lines) increases with  $l$  (diffuseness) while nickel oxidation introduces a translational descent (compression). In a simplest nickel oxide system, spatial and chemical factors decouple, enabling an approximated linear expression for the confinement radius parameter in DFTB as  $r_0 = \alpha l + \beta$ , where  $l$  denotes the lattice parameter,  $\alpha$  captures the spatial dependence, and  $\beta$  encodes the chemical oxidation state as shown by the dashed line connecting the {oxidation state, lattice constant} points. For more complex environments, this local form is expected to generalize into non-linear regression.